Effect of thermal boundary condition of an inner cube on three-dimensional natural convection in a cubical [†]

H. S. Yoon[1,*], J. H. Jung[2], H. S. Lee[2] and B. Y. Koo[3]

[1]*Global Core Research Center for Ships and Offshore Plants, Pusan National University, Jang Jeon 2-Dong, Geum Jeong Gu, Busan, 609-735, Korea*
[2]*Department of Naval Architecture and Ocean Engineering, Pusan National University, Jang Jeon 2-Dong, Geum Jeong Gu, Busan, 609-735, Korea*
[3]*Korea Energy Technology Center, ABS Busan Korea, 88-7, Jungang-dong 4-ga, Jung-gu, Busan, 600-014, Korea*

Abstract

We numerically investigated three-dimensional (3-D) natural convection in a vertical cubic enclosure with an inner cube for Rayleigh numbers (Ra) in the range of $10^3 \leq Ra \leq 10^6$. For the inner cube at the center, four different thermal boundary conditions (adiabatic, neutral, and hot and cold isothermal conditions) were considered in order to investigate their effect on flow and thermal fields. For $Ra = 10^3$ and $Ra = 10^4$, single circulation appears regardless of the thermal boundary condition of the inner cube. When $Ra = 10^5$ and $Ra = 10^6$, the combined effects of the inner cube as a bluff body and the thermal condition imposed on the inner cube on the fluid flow and thermal fields are significant, and intensify the 3-D effect. Generally, for $Ra = 10^5$ and $Ra = 10^6$, the convective flow is characterized by the formation of two inner vortices embedded in the primary circulation, and by secondary vortices due to flow separation at the edge of the inner body. As Ra increases, the local Nusselt number varies rapidly in the vertical direction, which is supported by the temperature isosurfaces that form an S-shape. The total surface-averaged Nusselt numbers for the different cases have approximately the same profile with respect to the Rayleigh number as the power function.

Keywords: Cubical enclosure; Inner cube; Three-dimensional natural convection; Thermal boundary condition effect

---

1. Introduction

The natural convection in an enclosure is relevant to many industrial and environmental applications such as heat exchangers, nuclear and chemical reactors, the cooling of electronic equipment, and stratified atmospheric boundary layers. In engineering applications, the geometries that arise in practice are more complicated than a simple enclosure filled with convective fluid [1-3]. A geometric configuration of interest includes the presence of bodies embedded within the enclosure. We investigated the natural convection in the annuli between an inner cube and an outer cubical enclosure with a vertically-imposed temperature difference. Thus, the 3-D natural convection in a vertical cubic enclosure without an inner body can be considered as an elementary problem and also a probem related to the present topic.

Mallinson and de Vahl Davis [4] numerically studied the 3-D natural convection in a rectangular cavity as a result of differential side heating. According to their calculations, the flow field in the cavity was strongly 3-D, with spiraling streamlines transporting fluid from the core to the side walls and back.

Hiller et al. [5] experimentally investigated thermal convection in a cubic cavity with two opposite vertical walls kept at prescribed temperatures. They considered high Prandtl numbers (from 5.8 to 6×10^3) and Rayleigh numbers ranging from 10^4 to 2×10^7. Thier experimental results showed that streamlines spiral from the foci on the walls toward the foci in the vertical midplane and vice versa, which is similar to the findings of Mallinson and de Vahl Davis [4]. Additionally, they observed the transition from one-roll to two-roll convection according to the Rayleigh number.

Fusegi et al. [6] numerically studied 3-D steady-state natural convection in a cubical enclosure for a Rayleigh number range of $10^3 \leq Ra \leq 10^6$. The enclosure was heated differentially at two vertical side walls. They considered the 3-D effect on the natural convection, particularly near the end walls in the transverse direction. As the Rayleigh number increased, the convective behavior intensified, and significant transverse variations tended to be confined into narrower areas close to the end walls.

Pallarès et al. [7] numerically characterized natural convection in the range of $3500 \leq Ra \leq 10000$ in a cubical cavity, where buoyancy was induced by imposing a moderate temperature difference between the heated bottom and the cooled

---

top plates with perfectly adiabatic vertical walls. They observed four different structures, and the existence of the four structures made the surface-averaged Nusselt number dependent on the pattern adopted by the flow.

Hernández and Frederick [8] studied numerically the effect of an enclosure's aspect ratio on the supercritical Rayleigh number ($Ra = 8 \times 10^3$). They found a new type of convective structure that exhibits a characteristic toroidal-like form, with flow descending near the four vertical edges and ascending at the central vertical axis of the cube. The overall Nusselt number changed continuously when the aspect ratio was increased.

Frederick and Quiroz [9] numerically studied the steady-state laminar natural convection in a cubical enclosure with a cold vertical wall and a hot square sector on the opposite wall. They showed that the flow pattern consists of a single symmetric circulation cell and thermally-stratified 3-D flow, and the circulation cell exhibited cross-sectional changes at a high Rayleigh number.

The other geometry relevant to the present study is a cube in a cubical enclosure with a vertically-imposed temperature difference. Ha and Jung [10] investigated the 3-D heat transfer and flow phenomena of natural convection in a vertical cubic enclosure within which a centered cubic heat-conducting body generated heat. The presence of a cubic conducting body in a cubic enclosure resulted in a larger variation of the local Nusselt number at the hot and cold walls in the z-direction, compared to cases without a cubic conducting body in the cubic enclosure. This indicates the existence of strongly three-dimensional natural convection with the conducting body.

Few studies have been performed on the effect of thermal boundary conditions imposed on the inner cube for 3-D natural convection in a vertical cubic enclosure. The inner cube is not calculated but treated a rigid wall, which means a non-conducting body and a no-heating condition.

Therefore, in the present study, we considered an inner cube that maintains adiabatic and isothermal thermal boundary conditions for different Rayleigh numbers in the range of 10^3 to 10^6. The flow structures and the characteristics of heat transfer, such as the distributions of the isothermal lines, local surface Nusselt numbers, and surface-averaged Nusselt numbers, are discussed with respect to the Rayleigh number and the thermal boundary conditions of the inner body. In addition, the results for the inner cube are compared to those without the inner cube to determine the effects of the inner cube's thermal condition on the fluid flow and heat transfer in the enclosure.

2. Computational details

A schematic of the system considered in the present study is shown in Fig. 1. The system consists of a cubic enclosure with sides of length L, within which a cube with sides of length W is centered.

The temperatures of the left- and right-side walls are maintained at T_h and T_c, respectively. The bottom, top, front-
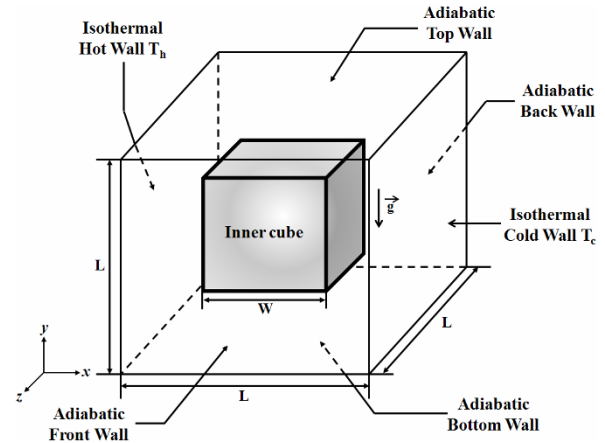

Fig. 1. Schematic of the system.

side, and rear-side walls are adiabatic. We assumed that the radiation effects can be taken to be negligible. The fluid properties are also assumed to be constant, except for the density in the buoyancy term, which follows the Boussinesq approximation. The gravitational acceleration acts in the negative y-direction. The immersed boundary method is used to handle the inner cube, which is located at the center of the enclosure in Cartesian coordinates. Therefore, the governing equations describing unsteady incompressible viscous flow and the thermal fields are the continuity, momentum, and energy equations in their non-dimensional forms, which are defined as

$$\frac{\partial u_i}{\partial x_i} - q = 0 \tag{1}$$

$$\frac{\partial u_i}{\partial t} + u_j \frac{\partial u_i}{\partial x_j} = -\frac{\partial P}{\partial x_i} + Pr \frac{\partial^2 u_i}{\partial x_j \partial x_j} + Ra Pr \Theta \delta_{i2} + f_i \tag{2}$$

$$\frac{\partial \Theta}{\partial t} + u_j \frac{\partial \Theta}{\partial x_j} = \frac{\partial^2 \Theta}{\partial x_j \partial x_j} + h . \tag{3}$$

The dimensionless variables in Eqs. (1)-(3) are defined as

$$t = \frac{t^* \alpha}{L^2}, \ x_i = \frac{x_i^*}{L}, \ u_i = \frac{u_i^* L}{\alpha}, \ P = \frac{P^* L^2}{\rho \alpha^2}, \ \Theta = \frac{T - T_c}{T_h - T_c} . \tag{4}$$

In the above equations, ρ, T and α represent the density, dimensional temperature, and thermal diffusivity, respectively. The superscript * in Eq. (4) represents the dimensional variables. x_i are Cartesian coordinates, u_i are the corresponding velocity components, t is the time, P is the pressure, and Θ is the temperature.

The preceding non-dimensionalization produces two dimensionless parameters, defined as $Pr = \frac{\nu}{\alpha}$ and $Ra = \frac{g \beta L^3 (T_h - T_c)}{\nu \alpha}$, where ν, g, and β are the kinematic viscosity, gravitational acceleration, and thermal expansion

coefficient, respectively. In our simulations, the Prandtl number Pr, and $r(=R/L)$, were taken to be 0.7 (corresponding to that of air) and 0.5, respectively. The Rayleigh number, Ra, varies in the range of $10^3 \sim 10^6$.

The mass source/sink q and momentum forcing f_i in Eqs. (1) and (2), respectively, were applied to the body surface, or inside the body, in order to satisfy the no-slip condition and mass conservation in the cell containing the immersed boundary. In Eq. (3), the heat source/sink h was applied to satisfy the isothermal boundary condition on the immersed boundary.

A two-step time-split scheme was used to advance the flow field. This scheme is based on the works of Kim and Moin [11] and Zang et al. [12]. First, the velocity was advanced from time level "n" to an intermediate level "*" by solving the advection-diffusion equation without the pressure term. In the advection-diffusion step, the nonlinear terms were treated explicitly using a third-order Adams-Bashforth scheme. The diffusion terms were treated implicitly using a Crank-Nicolson scheme. Then, the Poisson equation for pressure, which was derived by using mass conservation, was solved in a fully implicit manner. Once the pressure was obtained, the final divergence-free velocity field at "n+1" was obtained with a pressure-correction step. The temperature field was advanced in a manner similar to the third-order Adams-Bashforth scheme for the advection term, and the Crank-Nicolson scheme for the diffusion term.

A central difference scheme with second-order accuracy based on the finite volume method was used for spatial discretization. Additionally, a second-order linear or bilinear interpolation scheme was applied to satisfy the no-slip and isothermal conditions on the immersed boundary. Further details of the immersed-boundary method are given in Mohd-Yusof [13], Fadlun, et al. [14], Kim et al. [15] and Kim and Choi [16]. The present numerical methods were successfully used in the authors' previous studies of natural convection problems with a body in an enclosure for both the 2-D case [17-19] and the 3-D case [20].

For the velocity field, no-slip and no-penetration boundary conditions were imposed on the walls. Hot and cold wall temperatures of $\Theta = 1$ and 0 were imposed on the left and right walls of the enclosure, respectively, and the rest of the walls were considered to be adiabatic. For the thermal boundary condition of the inner cube at the center, we considered four different cases: an adiabatic body ($\partial\theta_{body}/\partial n = 0$), a neutral isothermal body ($\theta_{body} = 0.5$), a hot isothermal body ($\theta_{body} = 1$), and a cold isothermal body ($\theta_{body} = 0$), in order to investigate their effects on the flow and thermal fields in the system.

Once the velocity and temperature fields were obtained, the local and surface-averaged Nusselt numbers were defined, respectively, as

$$Nu = \frac{\partial\theta}{\partial n}\bigg|_{wall}, \quad \overline{Nu} = \frac{1}{S}\int_0^S Nu \, dS \quad (5)$$
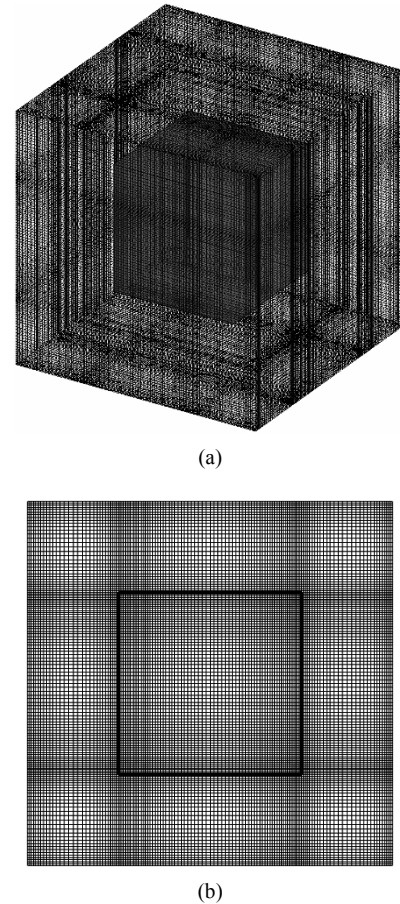
(a)

(b)

Fig. 2. Grid distribution of computational domain: (a) typical 3-D view; (b) 2-D (y, z)-plane view at $x = 0$ with non-uniform grid distribution.

where n is the normal direction to the walls and S is the surface area of the walls.

The typical 3-D view and 2-D (y, z)-plane view at $x = 0$ with nonuniform grid distribution are shown in Figs. 2(a) and 2(b), respectively. The inner cube in Fig. 2(a) and the square curve in Fig. 2(b) denote the immersed boundary. Further details of the method of handling arbitrarily complex 3-D immersed boundaries on Cartesian grids are given in Gilmanov et al. [21]. A grid resolution of $131 \times 131 \times 131$ along the x-, y- and z-directions was employed in our computations. The denser grids were uniformly distributed within the inner cube. The grid independence of the solution was tested with additional simulations on much finer grids, up to $201(x) \times 201(y) \times 201(z)$ points. The difference in the Nusselt number results obtained using the coarse and fine grids is less than 0.2%.

For the purpose of 3-D code validation, the natural convection problem in an enclosure without an inner cube in the center of the cubic enclosure was tested for Ra = 10^3, 10^4, 10^5, and 10^6 using a grid size of $131 \times 131 \times 131$ in the x-, y- and z-directions. The calculated average Nusselt numbers at the hot wall for the test cases were compared with the values
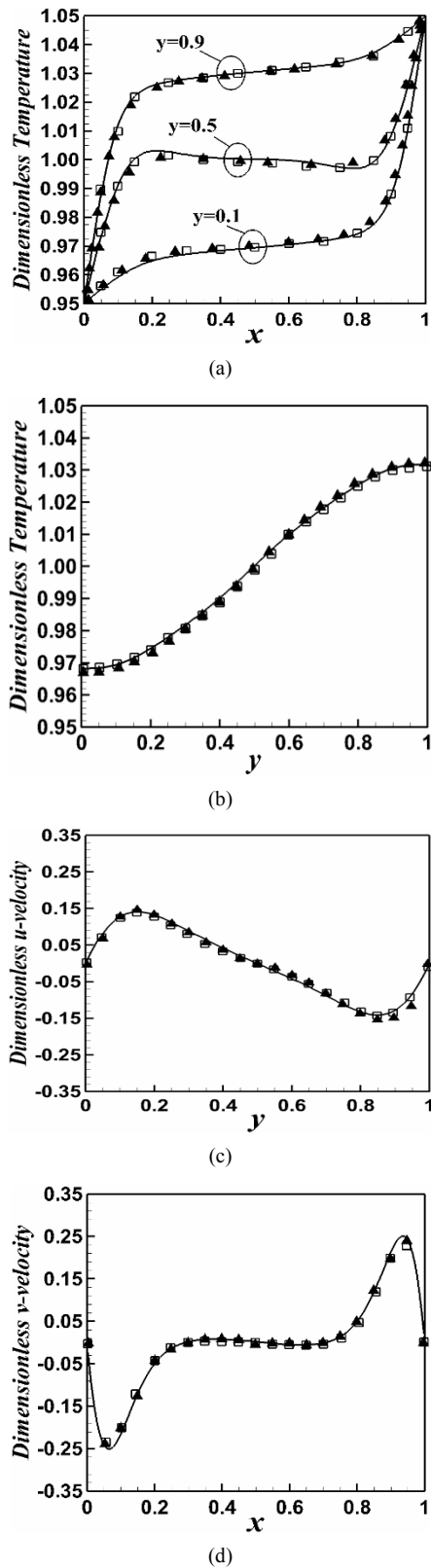
(a)

(b)

(c)

(d)

Fig. 3. Comparison of present results (shown in solid curves) for temperature and velocity profiles in the symmetry plane for $z = 0.5$ with results of Ha and Jung [11] (□) and Fusegi et al. [12] (▲) for Ra = 10^5: (a) results at various heights; (b) results at $x = 0.5$; (c) results at $x = 0.5$; (d) results at $y = 0.5$.

Table 1. Comparison of average Nusselt numbers at the hot wall with the values calculated in previous studies.

Ra	Average Nusselt number at the hot wall		
	This study	Ha and Jung [7]	Fusegi et al. [3]
10^3	1.044	1.072	1.085
10^4	1.925	2.070	2.100
10^5	4.329	4.464	4.361
10^6	8.656	-	8.770

calculated by Fusegi et al. [6] and Ha and Jung [10], where the Prandtl number was taken to be 0.7. As shown in Table 1, the calculated Nusselt numbers are in good agreement with the values calculated by Fusegi et al. [6] and Ha and Jung. [10]. In addition, the temperature and velocity profiles from the present calculation for Ra = 10^5 are in good agreement with the results obtained by Fusegi et al. [6] and Ha and Jung [10], as shown in Fig. 3.

3. Results and discussion

3.1 Flow and thermal fields

3.1.1 Case of Ra = 10^3

Fig. 4 shows the isotherms and superimposed streamlines in the cubic enclosure involving the inner cube with different thermal boundary conditions for $Ra = 10^3$ at z-plane locations of $z = 0.125$, $z = 0.5$ and $z = 0.875$.

For an adiabatic thermal boundary condition ($\partial\theta_{body}/\partial n = 0$) on the body, the streamlines at the $z = 0.125$ and 0.875 planes corresponding to the center plane of the front and rear channels are similar to the natural convection in a cubic enclosure without the inner body (Fusegi et al. [6]), which forms a single shell in the enclosure, as shown in Figs. 4(a) and 4(c), respectively. However, the streamlines on the midplane at the $z = 0.5$ do not form a single eddy with the center, due to the presence of the inner body, as shown in Fig. 4(b).

When $\theta_{body} = 0.5$, the flow circulates in the clockwise direction since the temperature of the inner cube is midway between the hot and cold wall temperatures on the left and right sides of the enclosure, respectively, regardless of the z-plane. Thus, the streamlines for $\theta_{body} = 0.5$ show almost the same distribution as those for $\partial\theta_{body}/\partial n = 0$, as shown in Figs. 4(d)-4(f). However, the diagonally symmetric shape of isotherms for $\partial\theta_{body}/\partial n = 0$ changes the fourfold symmetric shape about $x = 0$ and $y = 0$, regardless of the z variation, as shown in Figs. 4(d)-4(f), since the temperature of the inner cube is midway between the hot and cold wall temperatures.

Figs. 4(g)-4(i) show the isotherms and streamlines for different z-planes when $\theta_{body} = 1$. In general, the streamlines have the single circulating formation as the cases with $\theta_{body} = 0.5$ and $\partial\theta_{body}/\partial n = 0$. However, when the fluid moves away from the inner body and flows into the void
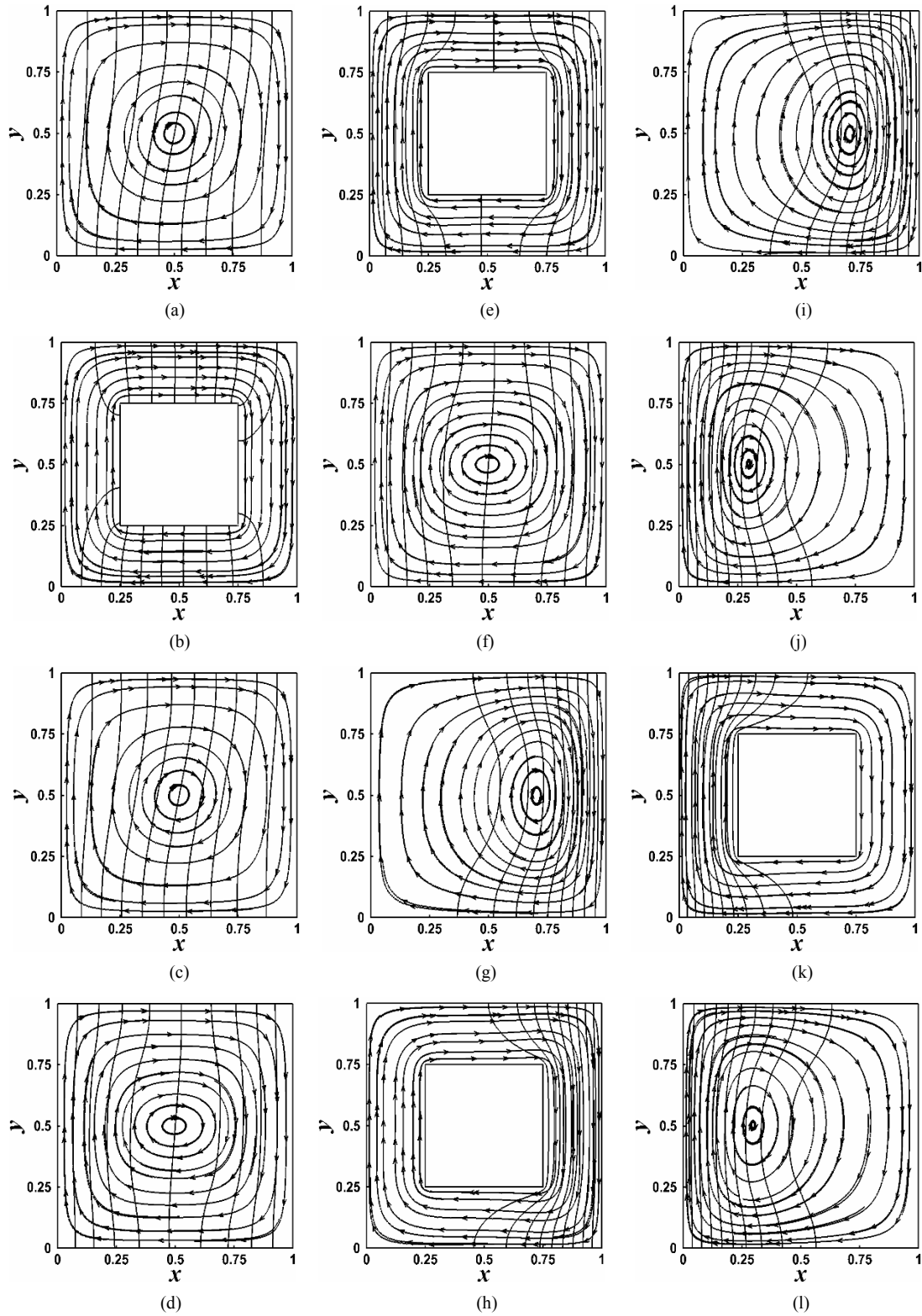
Fig. 4. 2-D isotherms and superimposed streamlines in cubic enclosure involving inner cube with different thermal boundary conditions for Ra = 10^3 at z = 0.125, 0.5, and 0.875: (a-c) $\partial\theta_{body} / \partial n$ = 0; (d-f) θ_{body} = 0.5; (g-i) θ_{body} = 1; (j-l) θ_{body} = 0.

space where the inner body does not interrupt the fluid flow, the center of the large eddy locates around the center of the right half of the enclosure. This change in the large eddy center is induced by the occurrence of a noticeable temperature variation only in the right half of the enclosure.

The temperature fields are symmetric across the horizontal centerline ($y = 0.5$). The variation of the isotherms almost limits in the right region which is bounded by the largest temperature difference between the right cold and hot side walls of the enclosure and the inner cube, respectively, regardless of the z-plane (see Figs. 4(g)-4(i)). Thus, the right channel between the right side walls of the enclosure and the inner cube forms a linear distribution of the temperature contours at $Ra = 10^3$, where conduction is the dominant mode of heat transfer. Otherwise, the left half of the enclosure is occupied by the hot fluids, resulting in no heat transfer since no isotherms exist in this region, as shown in Figs. 4(g)-4(i).

Figs. 4(j)-4(l) show the isotherms and streamlines for different z-planes when $\theta_{body} = 0$, corresponding to the case of a cold isothermal body. The shapes of isotherms and streamlines for $\theta_{body} = 0$ at $Ra = 10^3$, as shown in Figs. 4(j)-4(l), are similar to those for $\theta_{body} = 1$ at the same Rayleigh number shown in Figs. 4(g)-4(i), except that the isotherms and streamlines for $\theta_{body} = 0$ are symmetric with respect to the vertical centerline ($x = 0.5$) compared with those for $\theta_{body} = 1$.

3.1.2 Case of Ra = 10⁴

In the case of the adiabatic body, the circulation has a slightly elliptic shape with the axis rotating diagonally on the planes at $z = 0.125$ and $z = 0.875$, as shown in Figs. 5(a) and 5(c), respectively. Then, the isotherms for $\partial\theta_{body}/\partial n = 0$ circulate further in the clockwise direction by following the flow fields, regardless of the z-plane. Consequently, the isotherms in the left bottom and right top corner become denser than those in the case of $Ra = 10^3$. Simultaneously, the left top and the right bottom corners show coarser isotherms than in the case of $Ra = 10^3$. Otherwise, the diagonally symmetric isotherms and streamlines are maintained even as Ra increases from 10^3 to 10^4.

In the case of $\theta_{body} = 0.5$, when $Ra = 10^4$, the fourfold symmetric shape about $x = 0$ and $y = 0$ of isotherms at $Ra = 10^3$ broke and changed their shapes to diagonally symmetric ones, regardless of the z variation, as shown in Figs. 5(d)-5(f). This distribution of isotherms follows the single circu- lation of fluid flow due to increased convection with an increasing Rayleigh number. Eventually, the isotherms and streamlines reveal a distribution similar to that of the cases of $\partial\theta_{body}/\partial n = 0$.

For $\theta_{body} = 1$ and $\theta_{body} = 0$, the isotherms and streamlines on different z-planes for $Ra = 10^4$ are plotted in Figs. 5(g)-5(l), respectively. Because the isotherms follow this circulating flow, they rotate in the clockwise direction and change from a symmetric shape across the horizontal centerline ($y = 0.5$) at $Ra = 10^3$ to an asymmetric shape at $Ra = 10^4$. In addition, the center of the circulation slightly

inclines in the clockwise direction on the $z = 0.125$ and $z = 0.875$ planes, as shown in Figs. 5(g) and 5(i), respectively. Thus, for $\theta_{body} = 1$, the isotherms are more compressed toward the right upper side and more deflected toward the left lower side, as shown in Figs. 5(g)-5(i), compared with those at $Ra = 10^3$. Eventually, a hot zone is formed in the left upper region at $Ra = 10^4$, instead of in the left half of the enclosure at $Ra = 10^3$. For $\theta_{body} = 0$, the shapes of isotherms and streamlines, as shown in Figs. 5(j)-5(l), exhibit diagonal symmetry with respect to those of $\theta_{body} = 1$ at the same Rayleigh number (shown in Figs. 5(g)-5(i)). Thus, the cold zone appears in the right lower region.

3.1.3 Case of Ra = 10⁵

In general, at $Ra = 10^5$, the combined effects of the inner cube as a bluff body and the thermal condition imposed on the inner cube on the fluid flow and thermal fields are significant and intensify the 3-D effect compared to the case without the inner cube (Fusegi et al. [6]). Thus, the streamlines and isotherms strongly depend on the z-direction.

In the case of the adiabatic body, the large single eddy at $Ra = 10^3$ and $Ra = 10^4$ changes into two vortices at $Ra = 10^5$ in the side planes at $z = 0.125$ and $z = 0.875$, as shown in Figs. 6(a) and 6(c), respectively. The inner vortex remains elongated and eventually separates into two inner vortices, since strong flow limits near the vertical isothermal walls where the thermal boundary becomes noticeable. Simultaneously, the isotherms in the interior become more horizontally formed. This variation of the streamlines and isotherms according to the Rayleigh number is almost the same as in the case without an inner body.

Otherwise, on the mid-plane at $z = 0.5$, the flow circulates around the inner body without the inner vortex because of the presence of the inner body, as in the cases of lower Ra s. However, at this large value of $Ra = 10^5$, the secondary vortices newly appear on the side walls of the inner cube due to flow separation at the top right and bottom left corners of the inner cube, as shown in Fig. 6(b).

The shapes of streamlines and isotherms for $\theta_{body} = 0.5$, as shown in Figs. 6(d)-6(f), are similar to those for $\partial\theta_{body}/\partial n = 0$ except for the secondary vortices on the inner cube. The neutral isothermal condition of $\theta_{body} = 0.5$ fully satisfies the weak variation of temperature with the half value of the hot and cold isothermal conditions in the central region for the case without the inner cube.

For $\theta_{body} = 1$ and $\theta_{body} = 0$, the isotherms and streamlines in different z-planes at $Ra = 10^5$ are plotted in Figs. 6(g)-6(l), respectively. On the front and back channel center planes at $z = 0.125$ and $z = 0.875$ for $\theta_{body} = 1$, the circulation becomes more oblique and forms a triangular shape with the center close to the right lower corner. This is due to stronger circulation in the clockwise direction, as shown in Figs. 6(g) and 6(i), respectively. Thus, for $\theta_{body} = 1$, the isotherms are more compressed toward the right upper side and are then widely spread through the lower half of the
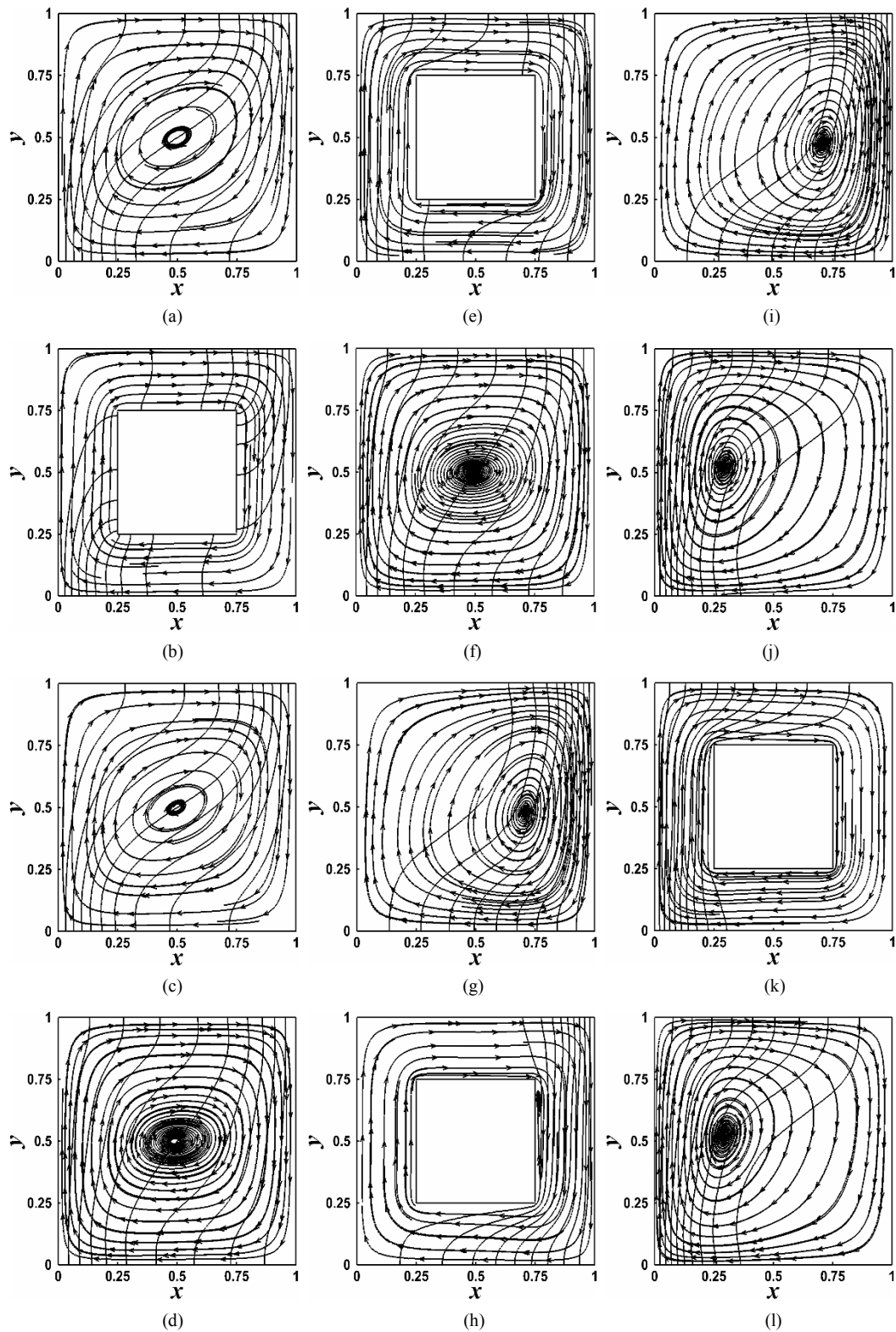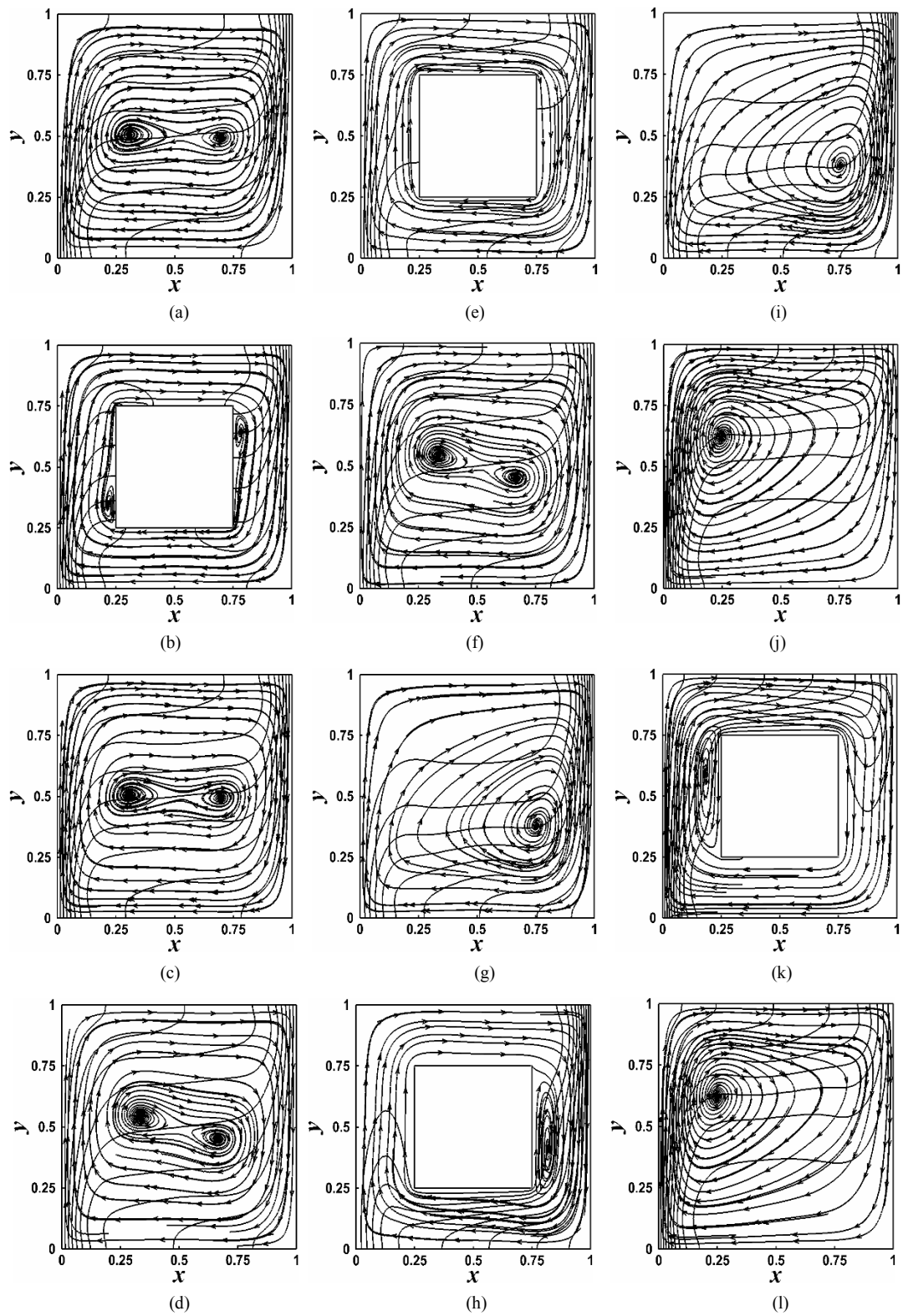
Fig. 5. 2-D isotherms and superimposed streamlines in cubic enclosure involving inner cube with different thermal boundary conditions for $Ra = 10^4$ at $z = 0.125$, 0.5, and 0.875: (a-c) $\partial\theta_{body} / \partial n = 0$; (d-f) $\theta_{body} = 0.5$; (g-i) $\theta_{body} = 1$; (j-l) $\theta_{body} = 0$.

Fig. 6. 2-D isotherms and superimposed streamlines in cubic enclosure involving inner cube with different thermal boundary conditions for $Ra = 10^5$ at $z = 0.125$, 0.5, and 0.875: (a-c) $\partial\theta_{body} / \partial n = 0$; (d-f) $\theta_{body} = 0.5$; (g-i) $\theta_{body} = 1$; (j-l) $\theta_{body} = 0$.

enclosure by a strong returning cold fluid flow. Consequently, the hot zone gradually shrinks with an increasing Rayleigh number.

In the mid-plane at $z = 0.5$ for $\theta_{body} = 1$, the isotherms form along the channel from the right top corner of the enclosure to the center ($y = 0.5$) of the left channel, as shown in Fig. 6(h). The strong circulating flow accelerates from the right top region with the sharp temperature gradient. Then, the flow is separated at the right top corner of the inner cube, forming a single secondary circulation on the right surface of the inner cube. The flow loses inertia and decelerates due to friction with the channel walls. Thus, flow separation does not occur at the other corners of the inner cube, as shown in Fig. 6(h). For $\theta_{body} = 0$, the shapes of the isotherms and streamlines shown in Figs. 6(j)-6(l) exhibit diagonal symmetry with respect to those for $\theta_{body} = 1$ at the same Rayleigh number shown in Figs. 6(g)-6(i).

3.1.4 Case of Ra = 10⁶

Figs. 7 and 8 show the streamlines and isotherms in the cubic enclosure with an inner cube with different thermal boundary conditions for $Ra = 10^6$ at $z = 0.125$, $z = 0.5$, and $z = 0.875$.

For $\partial\theta_{body}/\partial n = 0$, on the side planes in Figs. 7(a) and 7(c), the centers of the inner vortices for $Ra = 10^6$ are closer to the vertical isothermal walls than those for $Ra = 10^5$. Also, the vortices near the isothermal walls are more elongated along the vertical direction than those for $Ra = 10^5$. On the midplane ($z = 0.5$) in Fig. 7(b), the two inner vortices become larger and their length covers the side wall of the inner cube, since the formation of both inner vortices starts from the edge of the inner cube due to flow separation at the corresponding edge. This enlarged shape of the inner two vortices suggests that the inner two vortices in the midplane have the combined effects of the bluff body of the inner cube, and strong natural convection.

For $\theta_{body} = 0.5$, the centers of the inner vortices occur near the corners of the enclosure and almost on the diagonal line, as shown in Figs. 7(d)-7(f), compared to those on the horizontal line for $\partial\theta_{body}/\partial n = 0$ as shown in Figs. 7(a)-7(c). The different formation and location of the inner vortices between $\theta_{body} = 0.5$ and $\partial\theta_{body}/\partial n = 0$ is caused by the distribution of the isotherms. Namely, the deflection points of the isotherms appear near the left top and right bottom corners, which are away from the center ($y = 0$) as shown in Figs. 8(d)-8(f). This is because the isothermal condition of the inner cube with the medium temperature of the hot and cold walls contributes the temperature in the central region to be neutral. In addition, the isotherms near both corners are denser, with sharper gradients than those in the case of $\partial\theta_{body}/\partial n = 0$.

For $\theta_{body} = 1$ and $\theta_{body} = 0$, the streamlines and isotherms in different z-planes at $Ra = 10^6$ are plotted in Figs. 7(g)-7(l) and 8(g)-8(l), respectively. For $\theta_{body} = 1$, the hot right side wall of the inner cube and the cold right side wall of the enclosure form a narrow channel, and is predominant to

the convection temperature variation. Also, the intensity of the clockwise rotating circulation increases with an increasing Ra. Thus, on the midplane, as Ra increases, the inner vortex in the right channel becomes larger and its center moves slightly in the clockwise direction.

On the front or rear side of the enclosure, the inner vortex within the right channel shown on the midplane moves in the clockwise direction as the main circulation direction, leading to the center of the inner vortex moves downward in the channel and locates near the right corner. Also, the inner vortex reveals a horizontal formation and eventually separates into two vortices, as shown in Figs. 7(g) and 7(i), respectively. Finally, in the vicinity of the front and rear adiabatic walls, the inner vortices disappear (not shown here for the sake of brevity).

The thermal boundary layer on the right cold vertical wall is thinner than that on the left hot vertical wall because the hot right side wall of the inner cube and the cold right side wall of the enclosure form a narrow channel bounded by a large temperature difference. Also, because the intensity of the clockwise rotating circulation increases as the Rayleigh number increases, a temperature variation with a large deformation of the isotherms is noticeable in the region near the lower right corner of the enclosure.

3.2 Local Nusselt number and temperature isosurfaces

The local Nusselt number (Nu) distributions on the isothermal vertical wall at different thermal boundary conditions of the inner body for $Ra = 10^3$ are shown in Fig. 9. In addition, the temperature isosurfaces are plotted to identify the 3-D effect of the inner cube on convection and support the variation of the local Nusselt number distribution on the isothermal vertical walls in Fig. 9 where the distribution of Nu on the left hot wall is only presented.

In the case of $\partial\theta_{body}/\partial n = 0$, the large values of Nu on the left hot vertical wall locate near the bottom wall, as shown in Fig. 9(a), since the isotherms on the upper part lean slightly on the cold wall, due to the presence of a small fluid flow circulating in the clockwise direction. The convex shapes of the temperature isosurfaces are formed over both the hot and cold vertical walls, as shown in Fig. 9(b). However, the focuses of the convex isosurfaces over the hot and cold vertical walls are eccentric with respect to the horizontal center ($y = 0.5$), due to the clockwise circulation. Thus, the minimum of Nu on the hot wall appears at a location slightly over the horizontal center ($y = 0.5$) at the center of the z-direction ($z = 0.5$), respectively, as shown in Fig. 9(a).

For $\theta_{body} = 0.5$, Nu s on the hot wall reveal a radial distribution with the maximum at the center of the surface ($y = 0.5$, $z = 0.5$), as shown in Fig. 9(c). The isotherms are compressed into the hot and cold vertical walls by the presence of a neural isothermal inner body, resulting in denser isotherms in the left and right channels ($0 < z < 0.25$, $0.75 < z < 1$), as shown in Figs. 4(d)-4(f). Therefore, the concave shape of the tempera-
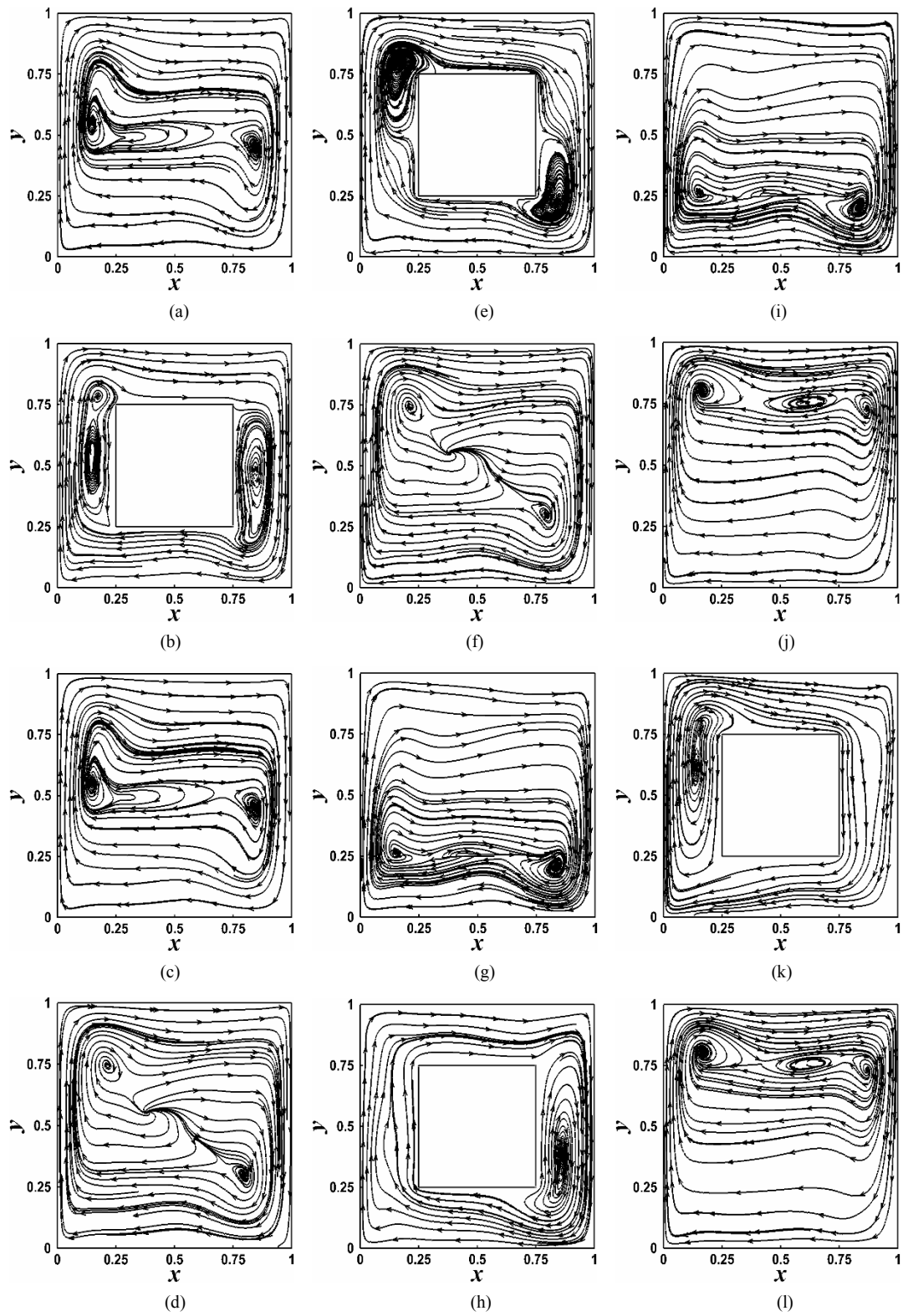
Fig. 7. Streamlines for Ra = 10^6 at z = 0.125, 0.5 and 0.875: (a-c) $\partial\theta_{body}\,/\,\partial n$ = 0; (d-f) θ_{body} = 0.5; (g-i) θ_{body} = 1; (j-l) θ_{body} = 0.

Fig. 8. Isothermals for $Ra = 10^6$ at $z = 0.125$, 0.5, and 0.875: (a-c) $\partial\theta_{body} / \partial n = 0$; (d-f) $\theta_{body} = 0.5$; (g-i) $\theta_{body} = 1$; (j-l) $\theta_{body} = 0$.
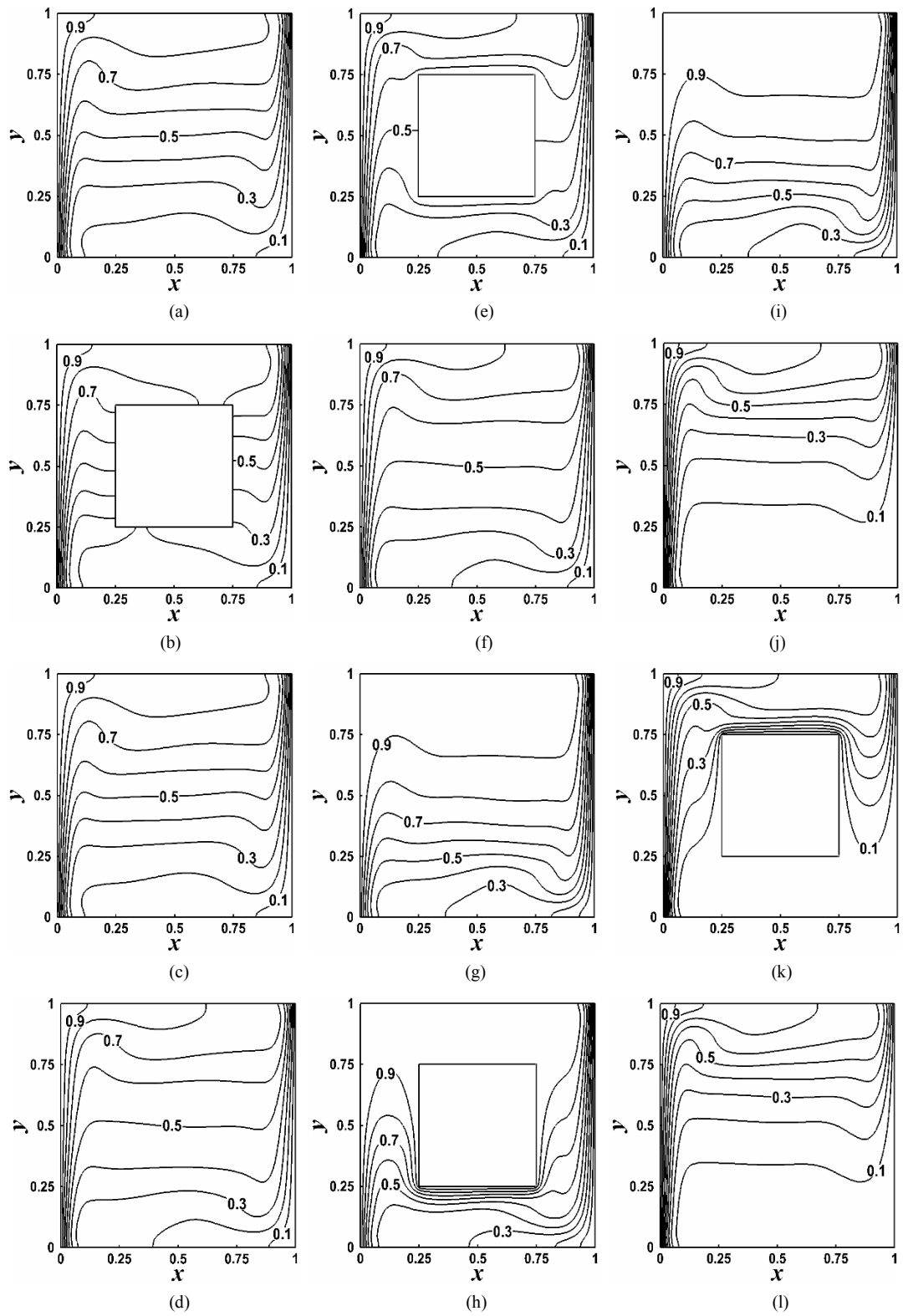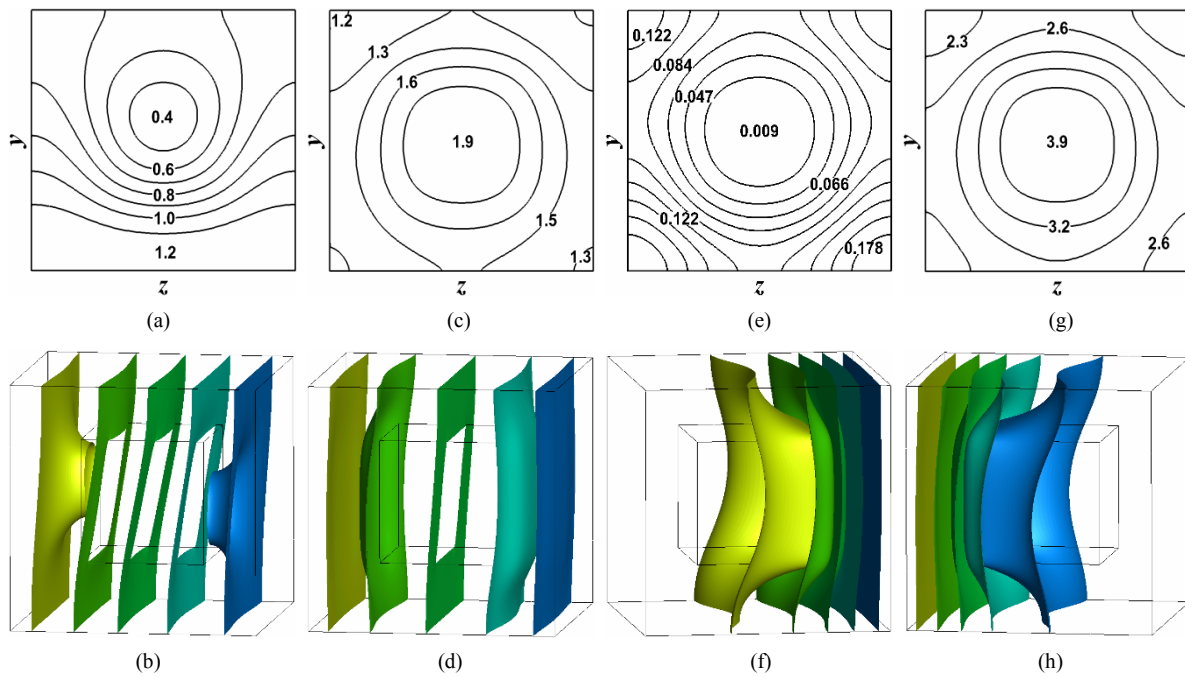
Fig. 9. Local Nusselt number distributions on isothermal vertical wall and temperature fields at different thermal boundary conditions of inner body for $Ra = 10^3$: (a-b) $\partial\theta_{body} / \partial n = 0$; (c-d) $\theta_{body} = 0.5$; (e-f) $\theta_{body} = 1$; (g-h) $\theta_{body} = 0$.

ture isosurfaces with their focus at the centers of the hot and cold walls ($y = 0.5$, $z = 0.5$) occurs as shown in Fig. 9(d), which supports the central location of the maximum local Nusselt number.

For $\theta_{body} = 1$ and $\theta_{body} = 0$, in general, Nu s on each wall present a similar radial distribution to $\theta_{body} = 0.5$, as shown in Figs. 9(e) and 9(g), respectively. The small Nu s with the minimum and large Nu s with the maximum distribute on the left hot and right cold walls for $\theta_{body} = 1$ and $\theta_{body} = 0$, as shown in Figs. 9(e) and 9(g), respectively. The large concave shapes of the temperature isosurfaces with their focus at the center in Figs. 9(f) and 9(h) support the presence of the maxima of Nu s at the centers of the corresponding walls.

When $Ra = 10^4$, for $\partial\theta_{body}/\partial n = 0$, the location of the minimum Nu s on the right hot wall moves to the top wall, as shown in Fig. 10(a), because stronger circulation lifts the isotherms containing relatively cold fluids. Thus, the small convex shape of the temperature isosurfaces appears near the top and bottom walls, regarding to the right hot and left cold vertical walls, respectively, as shown in Fig. 10(b). Otherwise, the maximum of Nu s appears in the vicinity of the bottom wall in the center of the z-direction ($z = 0.5$).

For $\theta_{body} = 0.5$, when $Ra = 10^4$, the maximum of Nu s occurs near the bottom and decreases as we moves from the bottom wall to the top wall where the minimum of Nu s appears, as shown in Fig. 10(c). The S-shape of the temperature isosurfaces near the isothermal vertical walls indicate the position of the maximum and the minimum Nu s, as shown in Fig. 10(d).

For $\theta_{body} = 1$, on the left wall, the smaller values of Nu s appear in the upper half of the surface, as shown in Fig. 10(e), which corresponds to the hot zone as observed in the distribution of isotherms. The Nu s on the right cold wall for $\theta_{body} = 1$ are much larger than those on the left hot wall. The maximum occurs near the top wall at $z = 0.5$, and decreases as we moves from the top wall to the bottom wall. The upside-down distribution of Nu s on the left hot wall for $\theta_{body} = 0$ in Fig. 10(g) corresponds to the distribution of Nu s on the right cold wall for $\theta_{body} = 1$. Thus, the radial distribution of Nu s on the isothermal walls at $Ra = 10^3$ does not appear at $Ra = 10^4$. Therefore, the S-shape of the temperature isosurfaces govern the distributions of Nu s on the isothermal walls, as shown in Figs. 10(f) and 10(h) for $\theta_{body} = 1$ and $\theta_{body} = 0$, respectively.

For $Ra = 10^5$, in the cases of $\partial\theta_{body}/\partial n = 0$ and $\theta_{body} = 0.5$, the distributions of Nu s show approximately the same pattern as those shown in Figs. 11(a) and 11(c), respectively. Namely, on the left hot wall, the maximum occurs near the center of the bottom, and its minimum appears near the top wall. In between the maximum and minimum values, Nu reveals an almost linear relation with respect to the y-direction. The distribution of Nu s on the right cold wall is an upside-down distribution of Nu s on the left hot cold (not shown in here for the sake of brevity). These similar distributions of Nu s between $\partial\theta_{body}/\partial n = 0$ and $\theta_{body} = 0.5$ originate from the S-shape of the isotherms, which can be identified by the temperature isosurfaces shown in Figs. 11(b) and 11(d), respectively.

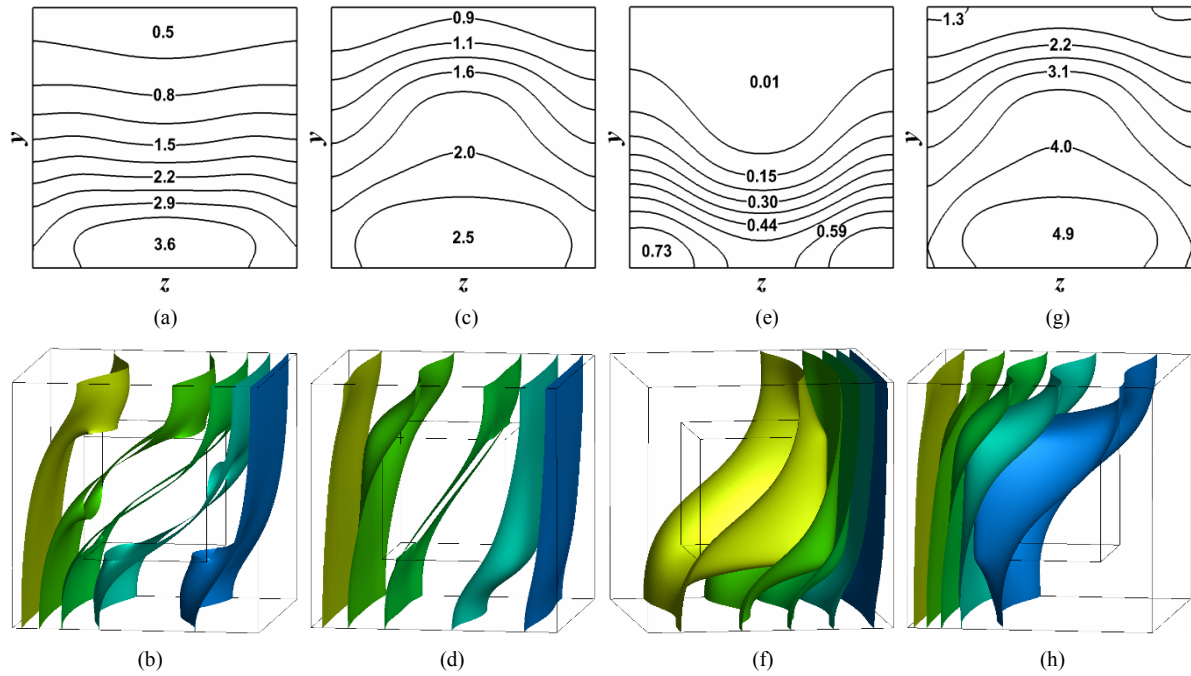For $\theta_{body} = 1$, because the clockwise circulation becomes

Fig. 10. Local Nusselt number distributions on isothermal vertical wall and temperature fields at different thermal boundary conditions of inner body for $Ra = 10^4$: (a-b) $\partial\theta_{body}/\partial n = 0$; (c-d) $\theta_{body} = 0.5$; (e-f) $\theta_{body} = 1$; (g-h) $\theta_{body} = 0$.
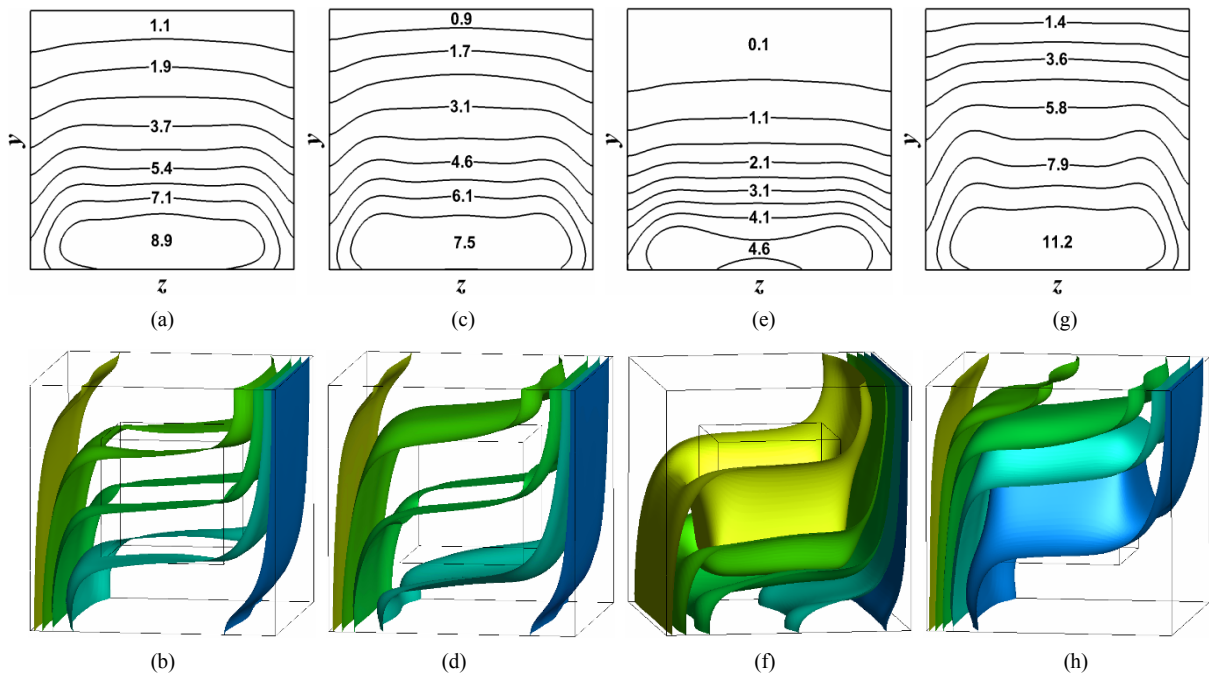

Fig. 11. Local Nusselt number distributions on isothermal vertical wall and temperature fields at different thermal boundary conditions of inner body for $Ra = 10^5$: (a-b) $\partial\theta_{body}/\partial n = 0$; (c-d) $\theta_{body} = 0.5$; (e-f) $\theta_{body} = 1$; (g-h) $\theta_{body} = 0$.

stronger, denser isotherms form in the regions near the left bottom and right top walls for $\theta_{body} = 1$. For $\theta_{body} = 0$, denser isotherms appear in the regions opposite to $\theta_{body} = 1$. Therefore, on the left hot wall, Nu has a maximum near the center of the bottom wall, and decreases in the upward direction, as shown in Figs. 11(e) and 15(g), respectively. On the

right cold wall, Nu has near the center of the top wall and decreases in the downward direction (not shown here for the sake of brevity). Thus, for $\theta_{body} = 1$ and $\theta_{body} = 0$, the S-shape is predominant to temperature isosurfaces, as shown in Figs. 11(f) and 11(h), respectively. In the hot and cold zones for $\theta_{body} = 1$ and $\theta_{body} = 0$, temperature isosurfaces rarely
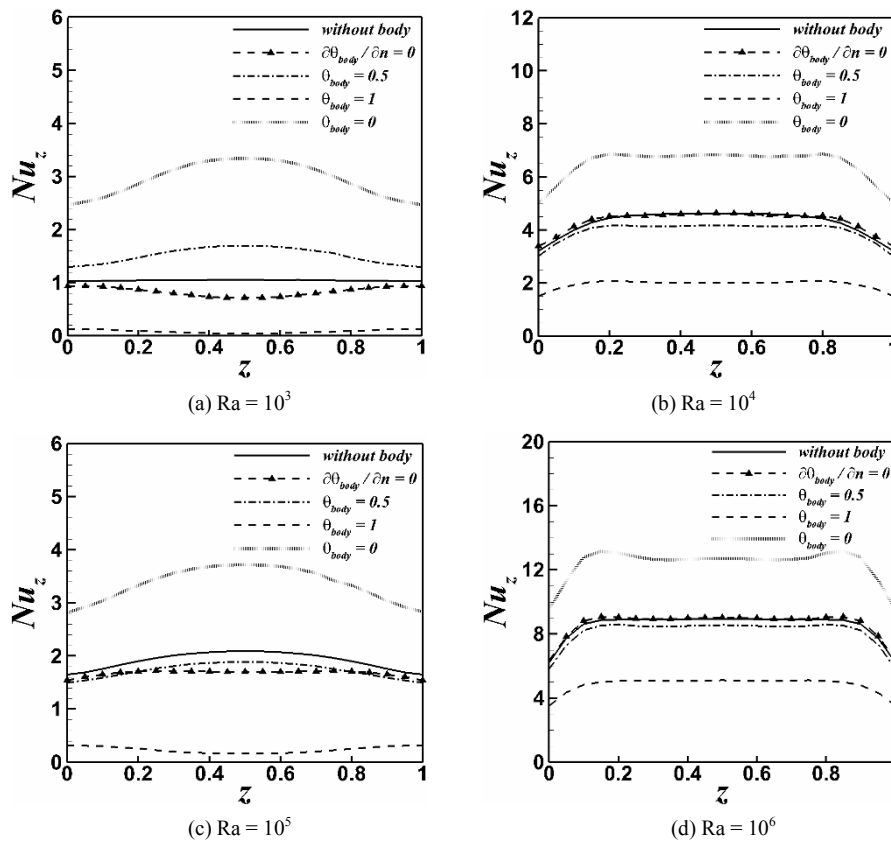
Fig. 12. Profiles of Nu_z for different boundary conditions at the hot wall for different Rayleigh numbers.

appear in one-half of the upper part of the left hot wall and one-half of the lower part of the right cold wall, respectively.

When $Ra = 10^6$, the distribution of the local Nusselt numbers on the isothermal vertical side walls shows the same pattern as that of the corresponding thermal condition of the inner cube for $Ra = 10^5$, which is not shown in here for the sake of brevity. In addition, the distributions of Nu for all thermal boundary conditions of the inner cube considered in this study reveal a similar pattern: Nu s are maximum near the center of the bottom, decrease in the increasing y-direction, and are eventually minimum near the top wall.

3.3 Line and surface-averaged Nusselt numbers

The local Nusselt numbers on the hot wall are averaged along the y-direction and then depend only on the z-direction, which are identified as follows:

$$Nu_z = \frac{1}{L_y} \int_0^{L_y} Nu\, dy \tag{6}$$

where L_y is the vertical length of the enclosure.

Fig. 12 shows the profiles of Nu_z for different thermal boundary conditions of the inner cube at different Rayleigh numbers. In general, the profiles of Nu_z along the z-direction are symmetric about the center of z ($z = 0.5$), regardless of the

thermal boundary of the inner cube and Ra. For $Ra = 10^3$, in the case without the inner body, the profile of Nu_z is independent of z, thereby identifying this case as a 2-D problem. In contrast to the case without the inner body, Nu_z depends on z, which confirms the existence of a 3-D effect in the presence of the inner cube regardless of the thermal boundary condition imposed on the inner body.

For $\partial \theta_{body}/\partial n = 0$, the minimum of Nu_z locates at $z = 0.5$ as shown in Fig. 12(a), due to the focus of the convex shape of the temperature isosurfaces over the hot wall. Otherwise, for $\theta_{body} = 0.5$, as z approaches from $z = 0$ and $z = 1$ to $z = 0.5$, Nu_z increases and reaches its maximum value, because the concave shape of the temperature isosurfaces with the focus at $z = 0.5$ results in the radial distribution of Nu s with a sharp temperature gradient at $z = 0.5$.

For $\theta_{body} = 1$, the values of Nu_z for all values of z are negligible on the left hot wall, since heat transfer rarely occurs in the left half of the enclosure bounded by the same thermal conditions imposed on the left hot wall and the inner body. For $\theta_{body} = 0$, as z approaches from $z = 0$ and $z = 1$ to $z = 0.5$, Nu_z increases and reaches its maximum, as shown in Fig. 12(a). In addition, at a fixed z, Nu_z for $\theta_{body} = 0$ reveals the largest value among the cases considered in this study. This profile of Nu_z on the left hot wall for $\theta_{body} = 0$ corresponds to that on the right cold wall for $\theta_{body} = 1$.

When $Ra = 10^4$, the profiles of Nu_z along z for each case

is similar to that at $Ra = 10^3$, which can be demonstrated by comparing Figs. 12(a) and 12(b) for $Ra = 10^3$ and $Ra = 10^4$, respectively. However, the magnitude of Nu_z increases due to augmentation of the convection by increasing the Rayleigh number.

When the Rayleigh number increases to $Ra = 10^5$ and $Ra = 10^6$, strong convection limits the sharp temperature gradient near the vertical walls and forms a thermal stratification in the interior. Thus, Rayleigh numbers $Ra = 10^5$ and $Ra = 10^6$ show the same pattern of Nu_z along z, independent of the inner cube and the thermal boundary conditions imposed on the inner cube. All cases reveal that Nu_z is invariant in the interior corresponding to $0.2 \le z \le 0.8$, and has a small value near the front and rear walls due to the effect of the adjacent adiabatic walls, as shown in Figs. 12(c) and 12(d) for $Ra = 10^5$ and $Ra = 10^6$, respectively.

Fig. 13 shows the surface-averaged Nusselt number of the hot wall ($\overline{Nu_H}$), the cold wall ($\overline{Nu_C}$), and the total surface-averaged Nusselt number ($\overline{Nu_T}$) as a function of the Rayleigh number for different thermal boundary conditions of the inner cube and the case without the inner cube. The cases of $\partial\theta_{body}/\partial n = 0$ and $\theta_{body} = 0.5$ exhibit almost the same profiles of $\overline{Nu_H}$ and $\overline{Nu_C}$ for the case without the inner body, as shown in Figs. 13(a) and 13(b), respectively.

At a fixed value of Ra, $\theta_{body} = 1$ and $\theta_{body} = 0$ present the smallest and the largest values of $\overline{Nu_H}$ among the present cases, as shown in Fig. 13(a). Regarding $\overline{Nu_C}$, the opposite is also true, as shown in Fig. 13(b). At $Ra = 10^3$, the $\overline{Nu_H}$ of $\theta_{body} = 1$ and $\theta_{body} = 0$ decreases and increases to about 100% and 180% of the case without the inner cube, respectively. As Ra increases, the difference becomes smaller for both $\theta_{body} = 1$ and $\theta_{body} = 0$, and reaches around 50% of the reduction and the augmentation, respectively.

The profiles of the total surface-averaged Nusselt number ($\overline{Nu_T}$) for the different cases almost overlap with each other, as shown in Fig. 13(c). The increment of $\overline{Nu_T}$ is governed by the power function of $\overline{Nu_T} = 0.1307 Ra^{0.304}$, which is the same as the function proposed by Fusegi et al. [6].

4. Conclusions

We investigated numerically the 3-D natural convection in a vertical cubic enclosure with an inner cube for different Rayleigh numbers in the range of $10^3 \le Ra \le 10^6$. For a thermal boundary condition of the inner cube at the center, four different thermal boundary conditions were examined: adiabatic ($\partial\theta_{body}/\partial n = 0$), neutral isothermal ($\theta_{body} = 0.5$), hot isothermal ($\theta_{body} = 1$), and cold isothermal ($\theta_{body} = 0$). These boundary conditions were used to investigate their effects on the flow and thermal fields in the system.
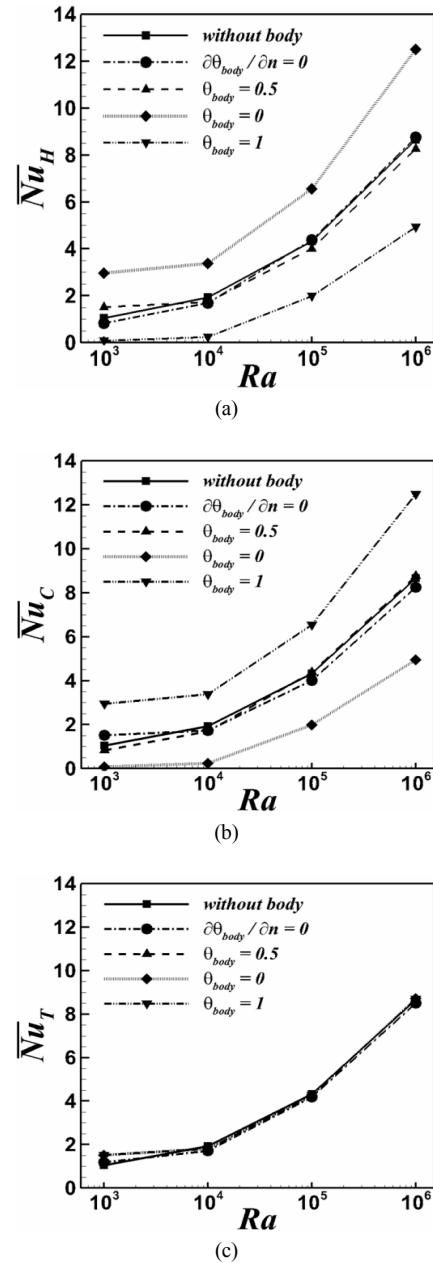

Fig. 13. Surface-averaged Nusselt number on isothermal vertical walls and total surface-averaged Nusselt number as a function of Rayleigh number for different thermal boundary conditions of the inner cube and the case without the inner cube: (a) hot wall; (b) cold wall; (c) total surface-averaged Nusselt number.

For $Ra = 10^3$, single circulation dominates the fluid flow for all thermal boundary conditions of the inner cube and the case without inner body, regardless of the relation to the z-plane. A single large circulation was maintained at $Ra = 10^4$, regardless of the thermal boundary condition of the inner cube. However, the formation has a slightly elliptic shape with the axis rotating diagonally, due to the enhancement of convection by increasing the Rayleigh number.

When $Ra = 10^5$ in the case without the inner body, the

convective flow is characterized by the formation of inner two vortices embedded in the primary circulation. For the case of the inner body at $Ra = 10^5$, the formation of streamlines is dependent on the inner cube. Thus, outside the inner body, the cases of $\partial\theta_{body}/\partial n = 0$ and $\theta_{body} = 0.5$ reveal the formation of two inner vortices embedded in the primary circulation. For $\theta_{body} = 1$ and $\theta_{body} = 0$, the circulation becomes more oblique and forms a triangular shape outside the inner body.

At the largest $Ra = 10^6$, in the case without the inner body, the formation of two inner vortices near the rear and front walls changes to four inner vortices. In the cases of $\partial\theta_{body}/\partial n = 0$, the isotherms and streamlines have distributions very similar to the case without the inner cube for $Ra = 10^6$. Otherwise, the case of $\theta_{body} = 0.5$ reveals the formation of two inner vortices regardless of the *z*-direction. For $\theta_{body} = 1$ and $\theta_{body} = 0$, in the region occupied by the inner body, the occurrence of flow separation forms a single secondary circulation. Outside the inner body, the inner vortex reveals a horizontal formation and eventually separates into two vortices.

The temperature isosurfaces show concave or convex shapes according to the thermal boundary condition of the inner body at $Ra = 10^3$. As the Rayleigh number increases, the S-shape of the temperature isosurfaces dominates the temperature distribution regardless of the thermal boundary condition of the inner body. Thus, the local Nusselt numbers on the hot wall have their maximum near the bottom wall and decrease along the vertical direction, independent of the Rayleigh number. The variation of the local Nusselt number along the *z*-direction is distinct only in the areas near the front and back walls.

The total surface-averaged Nusselt number ($\overline{Nu_T}$) for the different cases have about the same profile with respect to the Rayleigh number. The increment of $\overline{Nu_T}$ is governed by the power function.

Acknowledgment

References

[1] S. Roh and G. Son, Numerical study of natural convection in a liquefied natural gas tank, *J. Mech. Sci. Technol.*, 26 (10) (2012) 3133-3140.

[2] G. A. Sheikhzadeh, M. Nikfar and A. Fattahi, Numerical study of natural convection and entropy generation of Cu-water nanofluid around an obstacle in a cavity, *J. Mech. Sci. Technol.*, 26 (10) (2012) 3347-3356.

[3] G. F. Zheng, M. Y. Ha, H. S. Yoon and Y. G. Park, A numerical study on mixed convection in a lid-driven cavity with a circular cylinder, *J. Mech. Sci. Technol.*, 27 (1) (2013)

273-286.

[4] G. D. Mallinson and G. De Vahl Davis, Three-dimensional natural convection in a box: A numerical study, *J. Fluid Mech.*, 83 (1) (1977) 1-31.

[5] W. J. Hiller, S. Koch and T. A. Kowalewski, Three-dimensional structures in laminar natural convection in a cubic enclosure, Exp. *Therm. Fluid Sci.*, 2 (1) (1989) 34-44.

[6] T. Fusegi, J. Hyun, K. Kuwahara and B. Farouk, A numerical study of three-dimensional natural convection in a differentially heated cubical enclosure, Int. *J. Heat Mass Tran.*, 34 (6) (1991) 1543-1557.

[7] J. Pallarès, I. Cuesta, F. Grau and F. Giralt, Natural convection in a cubical cavity heated from below at low Rayleigh numbers, Int. *J. Heat Mass Tran.*, 39 (15) (1996) 3233-3247.

[8] R. Hernández and R. Frederick, Spatial and thermal features of three-dimensional Rayleigh-Bénard convection, *Int. J. Heat Mass Tran.*, 37 (3) (1994) 411-424.

[9] R. L. Frederick and F. Quiroz, On the transition from conduction to convection regime in a cubical enclosure with a partially heated wall, Int. *J. Heat Mass Tran.*, 44 (9) (2001) 1699-1709.

[10] M. Y. Ha and M. J. Jung, A numerical study on three-dimensional conjugate heat transfer of natural convection and conduction in a differentially heated cubic enclosure with a heat-generating cubic conducting body, Int. *J. Heat Mass Tran.*, 43 (23) (2000) 4229-4248.

[11] J. Kim and P. Moin, Application of a fractional step method to incompressible Navier-Stokes equations, *J. Comput. Phys.*, 59 (2) (1985) 308-323.

[12] Y. Zang, R. L. Street and J. R. Koseff, A non-staggered grid, fractional step method for time-dependent incompressible Navier–Stokes equations in curvilinear coordinates, *J. Comput.* Phys., 114 (1) (1994) 18-33.

[13] J. Mohd-Yusof, *Combined immersed-boundary/B-spline methods for simulations of flow in complex geometries*, Annual Research Briefs Center for Turbulence Research, NASA Ames and Stanford University (1997) 317.

[14] E. A. Fadlun, R. Verzicco, P. Orlandi and J. Mohd-Yusof, Combined immersed-boundary finite-difference methods for three-dimensional complex flow simulations, *J. Comput. Phys.*, 161 (2000) 35-60.

[15] J. Kim, D. Kim and H. Choi, An immersed-boundary finite volume method for simulations of flow in complex geometries, *J. Comput. Phys.*, 171 (1) (2001) 132-150.

[16] J. Kim and H. Choi, An immersed-boundary finite-volume method for simulation of heat transfer in complex geometries, *KSME International Journal*, 18 (6) (2004) 1026-1035.

[17] H. S. Yoon, M. Y. Ha, B. S. Kim and D. H. Yu, Effect of the position of a circular cylinder in a square enclosure on natural convection at Rayleigh number of 107, *Phys. Fluids*, 21 (4) (2009) 1-11.

[18] B. S. Kim, D. S. Lee, M. Y. Ha and H. S. Yoon, A numerical study of natural convection in a square enclosure with a circular cylinder at different vertical locations, *Int. J. Heat Mass Tran.*, 51 (7-8) (2008) 1888-1906.

[19] J. M. Lee, M. Y. Ha and H. S. Yoon, Natural convection in a square enclosure with a circular cylinder at different horizontal and diagonal locations, Int. *J. Heat Mass Tran.*, 53 (25-26) (2010) 5905-5919.

[20] H. S. Yoon, D. H. Yu, M. Y. Ha and Y. G. Park, Three-dimensional natural convection in an enclosure with a sphere at different vertical locations, *Int. J. Heat Mass Tran.*, 53 (15-16) (2010) 3143-3155.

[21] A. Gilmanov, F. Sotiropoulos and E. Balaras, A general reconstruction algorithm for simulating flows with complex 3D immersed boundaries on Cartesian grids, *J. Comput. Phys.*, 191 (2) (2003) 660-669.

Hyun Sik Yoon holds a position of Professor in Global Core Research Center for Ships and Offshore Plants at Pusan National University in the Korea. His research interests include flow control, heat and mixing enhancement, flow-structure interaction and biomimetics. He has authored over 100 publications in refereed journals and refereed proceedings of international conferences. He is also the recipient of numerous research grants from the National Science Foundation (NSF), other funding agencies as well as academic awards.